

# Thickness-dependent optical properties of layered hybrid organic-inorganic halide perovskites: A tight-binding GW-BSE study

Yeongsu Cho<sup>1</sup> and Timothy C. Berkelbach<sup>2,3</sup>

<sup>1</sup>*Department of Chemistry and James Franck Institute, University of Chicago, Chicago, Illinois 60637, USA*

<sup>2</sup>*Department of Chemistry, Columbia University, New York, New York 10027, USA*

<sup>3</sup>*Center for Computational Quantum Physics, Flatiron Institute, New York, New York 10010, USA\**

We present a many-body calculation of the band structure and optical spectrum of the layered hybrid organic-inorganic halide perovskites in the Ruddlesden-Popper phase with the general formula  $A'_2A_{n-1}M_nX_{3n+1}$ , focusing specifically on the lead iodide family. We calculate the mean-field band structure with spin-orbit coupling, quasiparticle corrections within the GW approximation, and optical spectra using the Bethe-Salpeter equation. The model is parameterized by first-principles calculations and classical electrostatic screening, enabling an accurate but cost-effective study of large unit cells and corresponding thickness-dependent properties. A transition of the electronic and optical properties from quasi-two-dimensional behavior to three-dimensional behavior is shown for increasing  $n$  and the nonhydrogenic character of the excitonic Rydberg series is analyzed. The thickness-dependent 1s and 2s exciton energy levels are in good agreement with recently reported experiments and the 1s exciton binding energy is calculated to be 302 meV for  $n = 1$ , 97 meV for  $n = 5$ , and 37 meV for  $n = \infty$  (bulk MAPbI<sub>3</sub>).

Hybrid organic-inorganic perovskites (HOIPs) are promising photovoltaic materials, most recently showing a high power conversion efficiency of over 24%.<sup>1</sup> A three dimensional bulk HOIP  $AMX_3$  can be transformed into a layered HOIP in the Ruddlesden-Popper phase  $A'_2A_{n-1}M_nX_{3n+1}$  by substituting a small organic cation  $A^+$  by a bulkier one  $A'^+$ . Common choices for the small organic cation are  $A^+ = CH_3NH_3^+$ ,  $NH_4^+$ ; for the bulkier cation are  $A'^+ = C_4H_9NH_3^+$ ,  $C_6H_5C_2H_4NH_3^+$ ; for the metal are  $M^{2+} = Sn^{2+}$ ,  $Pb^{2+}$ ; and for the halide are  $X^- = Cl^-$ ,  $I^-$ ,  $Br^-$ . A major drawback of the 3D HOIPs for photovoltaics is their relatively fast degradation when exposed to air, moisture, and light; in contrast, the layered HOIPs are more stable while maintaining high power conversion efficiencies under working conditions.<sup>2,3</sup> The optical properties of layered HOIPs can also be easily controlled by composition,<sup>4</sup> enhancing their flexibility for a variety of optoelectronic applications. Unlike the van der Waals materials – a prototypical family of layered materials including graphene, hexagonal boron nitride, and the transition-metal dichalcogenides – the layered HOIPs have sublayers that are covalently bonded. This distinct property makes the layered HOIPs an insightful mixed-dimensional platform for investigating the transition of optoelectronic properties from two dimensional to three dimensional.

The  $n$ -dependent properties of layered HOIPs have been experimentally investigated, especially during the last five years,<sup>5–9</sup> including mechanically exfoliated thin sheets of a layered HOIP.<sup>10,11</sup> Early theoretical investigations of the optical properties of layered HOIPs were performed using the effective mass approximation, giving good estimates for the exciton binding energy and a qualitative explanation of the essential physics.<sup>5,12–14</sup> For a quantitative analysis, *ab initio* approaches such as density functional theory (DFT) have been applied to study some  $n$ -dependent electronic properties<sup>15</sup> and were employed to build a semi-empirical model of an exciton incorporating heterogeneous dielectric screening.<sup>9</sup> The GW approximation combined with the Bethe-Salpeter equation

(BSE) represents a standard many-body approach for the accurate determination of the band structure and optical properties of semiconductors. While the 3D HOIPs have been extensively studied with the GW approximation,<sup>16–20</sup> the analogous calculation for the layered HOIPs is formidable due to the large number of atoms in the unit cell. Recently, by replacing the organic  $A'^+$  by a simpler cation,  $Cs^+$ , a GW-BSE calculation has been performed on cubic  $Cs_2PbI_4$ ,<sup>21</sup> corresponding to the  $n = 1$  all-inorganic layered lead-halide perovskite. For an overview of recent progress on low dimensional hybrid perovskites, including their structural and electronic properties, we refer to the excellent review by Katan, Mercier, and Even.<sup>22</sup>

In this work, we pursue a semiempirical GW-BSE approach in order to study the large unit cells encountered in layered HOIPs. Our approach differs from previous theoretical works because it is almost entirely parameterized by first-principles calculations and because the mean-field, self-energy, and exciton problems are treated on equal footing with atomistic detail, avoiding any effective mass approximations. However, compared to fully *ab initio* approaches, ours is computationally efficient due to the tight-binding parameterization and classical treatment of electrostatic screening. The results will be validated against recently obtained experimental data. We analyze the orbital character of the transitions, the dimensionality-dependent nonhydrogenic Rydberg series of the excitons, and present a term-by-term analysis of the carrier confinement and electrostatic effects that determine the optical properties of the layered HOIPs.

As depicted in Fig. 1, we assume a layered HOIP  $A'_2A_{n-1}M_nX_{3n+1}$ , which has alternating layers composed of organic spacers  $A'^{2+}$  and primarily-inorganic perovskites  $A_{n-1}M_nX_{3n+1}^{2-}$ . The organic cations  $A$  and  $A'$  primarily determine the structure and do not participate in the valence chemical bonding.<sup>23</sup> Therefore, our tight binding model is constructed based on the metal-halide perovskite structure  $M_nX_{3n+1}$ . Furthermore, due to the long organic spacers, we neglect the hybridization between perovskite layers.<sup>8,24</sup> For

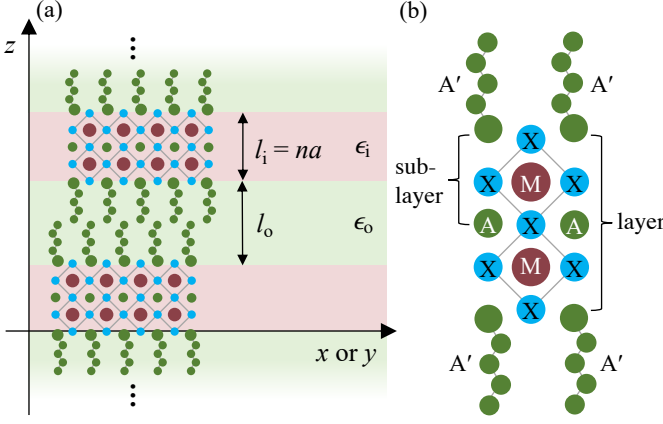


FIG. 1. (a) The electrostatic model of a layered HOIP, with  $n = 2$  shown as an example. For the case of  $(\text{C}_4\text{H}_9\text{NH}_3)_2(\text{CH}_3\text{NH}_3)_{n-1}\text{Pb}_n\text{I}_{3n+1}$ ,  $a = 6.39 \text{ \AA}$ ,<sup>28</sup>  $l_0 = 8.81 \text{ \AA}$ ,<sup>13</sup>  $\epsilon_i = 6.1$ ,<sup>29</sup> and  $\epsilon_0 = 2.1$ .<sup>29</sup> (b) A schematic representation of the structure of the layered HOIP depicted in (a). A is a small organic ammonium cation, A' is a bulky organic ammonium cation, M is a metal cation, and X is a halogen anion.

simplicity, we assume a cubic perovskite structure (space group  $Pm\bar{3}m$ ), such that  $\text{M}_n\text{X}_{3n+1}$  is modeled as  $n$  sublayers of the cubic  $\text{MX}_3$  with an additional X on the boundary. This approximation precludes a study of the Rashba effect,<sup>25,26</sup> arising from the inversion symmetry breaking of the typical orthorhombic structure,<sup>7</sup> although this effect could be straightforwardly included along the lines of Ref. 27. Henceforth, we will focus our attention on the specific case of layered HOIPs made from the popular parent compounds of ammonium or methylammonium (MA) lead iodide using butylammonium spacers, i.e.  $\text{A}'^+ = \text{C}_4\text{H}_9\text{NH}_3^+$ ,  $\text{A}^+ = \text{NH}_4^+$  or  $\text{CH}_3\text{NH}_3^+$ ,  $\text{M} = \text{Pb}$ , and  $\text{X} = \text{I}$ .

With the above approximations, we construct a tight-binding model in the basis of the atomic orbitals corresponding to the Pb 6s and 6p orbitals and the I 5s and 5p orbitals. This approach has been successfully applied to the 3D HOIPs, in order to study a variety of effects including the Rashba splitting,<sup>25,26</sup> the dependence of electronic properties on the atomic structure,<sup>27,30</sup> and dynamic properties.<sup>31</sup> The parameters of our tight-binding model are determined from a single DFT calculation on the cubic crystal structure; for simplicity, we perform calculations on  $\text{CsPbI}_3$ , whose lattice constant is very similar to that of cubic  $\text{MAPbI}_3$  and  $\text{NH}_4\text{PbI}_3$  (all between  $6.2 - 6.3 \text{ \AA}$ ). DFT calculations were performed using Quantum Espresso<sup>32</sup> with the PBE exchange correlation functional<sup>33</sup> and tight-binding matrix elements were determined using the Wannier90 code.<sup>34</sup> From these calculations, a number of symmetry unique real-space matrix elements (which extend beyond nearest-neighbor) can be determined and used to build a tight-binding representation for any *layered* HOIP structure. Importantly, this construction captures the carrier confinement (kinetic energy) effect arising in nanostructured materials.

Next, we include the spin-orbit coupling (SOC), which is extremely large because of the high atomic numbers of Pb and

I.<sup>35</sup> Including SOC requires two spin-orbital basis functions for each atomic spatial orbital leading to eight spin-orbitals for each Pb atom and eight spin-orbitals for each I atom. Following Ref. 25, we add two on-site Hamiltonians for the Pb and I p orbitals, each of the form

$$h^{\text{SOC,B}} = \frac{\Delta_{\text{SOC}}^{\text{B}}}{3} \begin{pmatrix} 0 & -i & 0 & 0 & 0 & 1 \\ i & 0 & 0 & 0 & 0 & -i \\ 0 & 0 & 0 & -1 & i & 0 \\ 0 & 0 & -1 & 0 & i & 0 \\ 0 & 0 & -i & -i & 0 & 0 \\ 1 & i & 0 & 0 & 0 & 0 \end{pmatrix}, \quad (1)$$

where the basis is ordered as  $\{|p_x \uparrow\rangle, |p_y \uparrow\rangle, |p_z \uparrow\rangle, |p_x \downarrow\rangle, |p_y \downarrow\rangle, |p_z \downarrow\rangle\}$  and where  $\Delta_{\text{SOC}}^{\text{B}}$  is the spin-orbit coupling constant of atom type B. We emphasize that we do not treat SOC perturbatively because of the large magnitude and the resulting bands have mixed spin character, i.e.  $S_z$  is not a good quantum number.

Combining the DFT and SOC matrix elements produces the total  $\mathbf{k}$ -dependent mean-field tight-binding Hamiltonian with matrix elements,

$$h_{\lambda\mu}^{\text{DFT+SOC}}(\mathbf{k}) = \sum_{\mathbf{T}} e^{i\mathbf{k}\cdot\mathbf{T}} h_{\lambda 0, \mu \mathbf{T}}^{\text{DFT}} + h_{\lambda 0, \mu 0}^{\text{SOC,Pb}} + h_{\lambda 0, \mu 0}^{\text{SOC,I}} \quad (2)$$

where  $\lambda$  and  $\mu$  are the atomic spin-orbital types and  $\mathbf{T}$  is a lattice translation vector. Diagonalization of this mean-field Hamiltonian yields an approximate layered HOIP band structure with SOC included nonperturbatively. However, the DFT band gap is a poor approximation to the true quasiparticle band gap, which can be estimated using the GW approximation to the self-energy.

The GW approximation to the self-energy,  $\Sigma = i\text{GW}$ , requires the screened Coulomb interaction  $W$ , which is typically calculated within the random-phase approximation.<sup>36-40</sup> Building  $W$  in this manner is responsible for the cost of GW calculations. Instead, we employ a few parameters that correct the 3D bulk band structure of the parent HOIP and then we appeal to a classical electrostatic treatment of screening in order to calculate the *change* in the self-energy due to a different dielectric environment (as realized in layered structures).

First, for the bulk correction, we identify five symmetry-distinct orbital types, corresponding to the Pb s orbitals, the Pb p orbitals (all three equivalent), the I s orbitals, the I p orbitals that are perpendicular to the Pb-I-Pb bond and the I p orbitals that are parallel to the Pb-I-Pb bond. For each of these atom types, we introduce a constant self-energy  $\Sigma_{\mu}$ , all of which are added to the diagonal of the above DFT+SOC Hamiltonian, in order to create an approximate GW Hamiltonian for the *bulk* HOIP,

$$h_{\lambda\mu}^{\text{GW}}(\mathbf{k}) = h_{\lambda\mu}^{\text{DFT+SOC}}(\mathbf{k}) + \Sigma_{\lambda} \delta_{\lambda\mu} \quad (3)$$

with band energies  $\varepsilon(\mathbf{k})$  and eigenvectors  $\mathbf{C}(\mathbf{k})$  determined by

$$\mathbf{h}^{\text{GW}}(\mathbf{k})\mathbf{C}(\mathbf{k}) = \mathbf{C}(\mathbf{k})\varepsilon(\mathbf{k}). \quad (4)$$

These five self-energies  $\Sigma_{\mu}$ , the above two SOC constants  $\Delta_{\text{SOC}}^{\text{B}}$ , and a single rigid “scissors”-style shift of the conduction band  $\Sigma_{\text{CB}}$  are then optimized in order to best reproduce the *ab initio* GW band structure of  $\text{MAPbI}_3$  presented

in Ref. 16, which also included SOC. The resulting band structure is shown in Fig. 2 with a band gap of 1.67 eV and an effective mass of  $0.20m_0$  for both the electron and the hole. The excitonic reduced mass of  $0.10m_0$  is consistent with the value determined by magneto-absorption experiments,  $0.104m_0$ .<sup>41</sup> The spin-orbit coupling constants are determined to be  $\Delta_{\text{SOC}}^{\text{Pb}} = 1.18$  eV and  $\Delta_{\text{SOC}}^{\text{I}} = 1.06$  eV, which are similar to the values used in a previous tight-binding study.<sup>27</sup>

Moving on to layered HOIPs, we model the system as a stack of alternating organic and inorganic slabs, each with a uniform dielectric constant as shown in Fig. 1. The screened Coulomb interaction between two charges placed on the planes at  $z_1$  and  $z_2$  and separated by the in-plane coordinate  $\rho$ ,  $W(\rho, z_1, z_2)$ , can be obtained in a closed form when the number of layers is infinite<sup>13,42</sup> or via the electrostatic transfer matrix method<sup>43</sup> when the number of layers is finite. Relative to the bulk self-energy, the *change* in the electrostatic self-energy of a charge in the inorganic section of a layered HOIP at height  $z$  is given by<sup>44,45</sup>

$$\delta\Sigma(z) = \frac{1}{2} \lim_{\rho \rightarrow 0} \left[ W(\rho, z_1 = z_2 = z) - \frac{1}{\epsilon_i \rho} \right], \quad (5)$$

where  $\epsilon_i$  is the dielectric constant of the inorganic section.

In the spirit of the conventional one-shot application of the GW approximation, we correct our bulk band structure using  $\delta\Sigma(z)$  via perturbation theory. Specifically, we assign the  $z$ -dependent self-energy shift to all atoms  $\mu$  at the height  $z_\mu$  and for each band we correct the eigenvalues with an expectation value,

$$E_c(\mathbf{k}) = \varepsilon_c(\mathbf{k}) + \delta\Sigma_c(\mathbf{k}) = \varepsilon_c(\mathbf{k}) + \sum_{\mu} |C_{\mu c}(\mathbf{k})|^2 \delta\Sigma(z_\mu) \quad (6a)$$

$$E_v(\mathbf{k}) = \varepsilon_v(\mathbf{k}) + \delta\Sigma_v(\mathbf{k}) = \varepsilon_v(\mathbf{k}) - \sum_{\mu} |C_{\mu v}(\mathbf{k})|^2 \delta\Sigma(z_\mu) \quad (6b)$$

where  $c$  and  $v$  index the spin-orbital conduction and valence bands (which have mixed spin character). In Fig. 2, we compare the bulk band structure to that obtained for the layered HOIP with  $n = 10$ . As expected, the latter has about the same band gap, but a ten-fold band multiplicity that tracks the dispersion of the bulk band structure.

To simulate the optical spectrum, we solve the Bethe-Salpeter equation (BSE) based on the GW self-energy.<sup>46–51</sup> The BSE, in the Tamm-Dancoff approximation, follows from the wavefunction ansatz

$$|\Psi_X\rangle = \sum_{cv} \sum_{\mathbf{k}} A_{cv}^X(\mathbf{k}) a_{c,\mathbf{k}}^\dagger a_{v,\mathbf{k}} |0\rangle, \quad (7)$$

where the exciton wavefunction  $A_{cv}^X(\mathbf{k})$  and excitation energy  $E_X$  are determined by the eigenvalue equation

$$E_X A_{cv}^X(\mathbf{k}) = [E_c(\mathbf{k}) - E_v(\mathbf{k})] A_{cv}^X(\mathbf{k}) - \sum_{c'v'} \sum_{\mathbf{k}'} (c\mathbf{k}, c'\mathbf{k}' | v'\mathbf{k}' v\mathbf{k})_W A_{c'v'}^X(\mathbf{k}'), \quad (8)$$

where we have neglected the excitonic exchange interaction. The two-electron integral associated with the screened

Coulomb interaction is

$$(c\mathbf{k}, c'\mathbf{k}' | v'\mathbf{k}' v\mathbf{k})_W = \sum_{\lambda\mu} C_{\lambda c}^*(\mathbf{k}) C_{\mu c'}^*(\mathbf{k}') C_{\mu v}(\mathbf{k}) C_{\lambda v'}(\mathbf{k}') \times W(|\mathbf{k} - \mathbf{k}'|, z_\lambda, z_\mu). \quad (9)$$

Here,  $W(k, z_1, z_2)$  is the in-plane Fourier-transformed screened Coulomb interaction obtained from the classical electrostatic problem described in the previous section. Furthermore, we have approximated the two-electron integrals in the localized atomic-orbital basis by neglecting differential overlap,  $\phi_\lambda^*(\mathbf{r}) \phi_\mu(\mathbf{r}) d\mathbf{r} \approx \delta_{\lambda\mu} |\phi_\mu(\mathbf{r})|^2 d\mathbf{r}$ .

Based on the solutions of the BSE, we calculate the linear absorption via the usual Fermi's golden rule, leading to

$$I(\omega) \propto \sum_X \left| \sum_{cv} \sum_{\mathbf{k}} A_{cv}^X(\mathbf{k}) \boldsymbol{\lambda} \cdot \mathbf{p}_{cv}(\mathbf{k}) \right|^2 \delta(\hbar\omega - E_X), \quad (10)$$

where  $\boldsymbol{\lambda}$  is the polarization of the light and  $\mathbf{p}_{cv}$  are transition matrix elements of the momentum operator. The momentum matrix elements are obtained via the commutation relation  $\mathbf{p}(\mathbf{k}) = (-im/\hbar)[\mathbf{r}, H]$  as follows<sup>52</sup>

$$\mathbf{p}_{cv}(\mathbf{k}) = \frac{m}{\hbar} [\nabla_{\mathbf{k}} \mathbf{h}^{\text{GW}}(\mathbf{k})]_{cv} + i \frac{m}{\hbar} [E_c(\mathbf{k}) - E_v(\mathbf{k})] \sum_{\lambda\mu} \mathbf{r}_{\lambda\mu} C_{\lambda c}^*(\mathbf{k}) C_{\mu v}(\mathbf{k}) \quad (11)$$

where the tight-binding dipole matrix elements  $\mathbf{r}_{\lambda\mu}$  are also obtained from Wannier90. We emphasize that this approach includes both inter- and intra-atomic transitions.

All BSE results shown are calculated on an  $N_k \times N_k$  Monkhorst-Pack mesh with  $N_k = 50 - 70$ , for which the first few excitation energies are well-converged. The BSE Hamiltonian is constructed using two valence bands and two conduction bands. In our testing, this approximation introduces

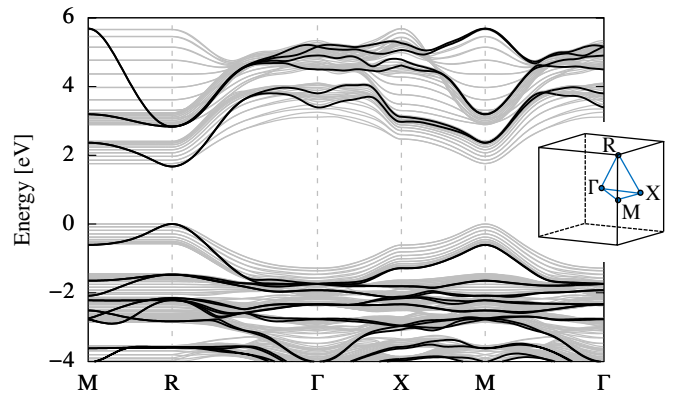


FIG. 2. Band structure of the 3D HOIP calculated by the tight binding method including the spin-orbit coupling and the GW self-energy correction using Eq. 3. Grey curves show the band structure of the layered HOIP with  $n = 10$  calculated using Eq. 6. The cubic Brillouin zone is shown along with high symmetry points and  $k$ -point path; note that in the  $n = \infty$  supercell limit, the M and R points become equivalent.

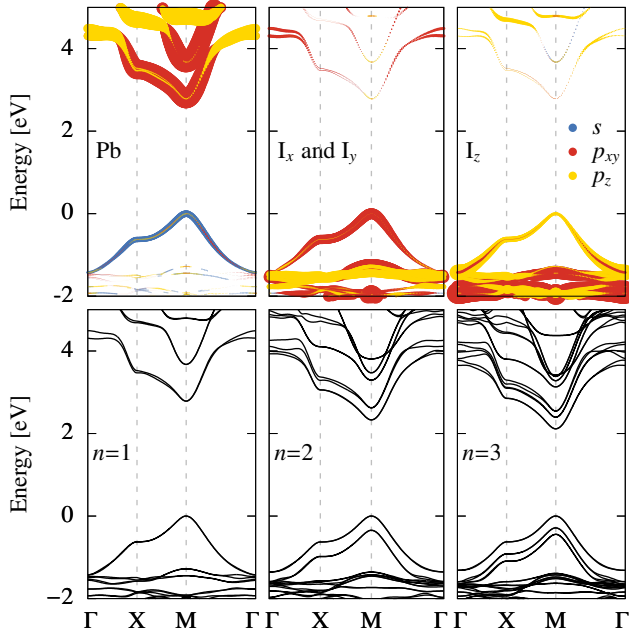


FIG. 3. Band structures calculated by Eq. 6. The top row shows orbital-projected band structures of  $n = 1$  for each atom and orbital type, where the line width is proportional to the contribution. The red lines for  $p_{xy}$  are the sum of the  $p_x$  and  $p_y$  orbital contributions. The bottom row shows the band structures of  $n = 1, 2$ , and  $3$ .

an error of less than 0.01 eV in the absolute value of the excitation energies. Importantly, our calculations account for the band structure throughout the Brillouin zone, which means that nonparabolicity is explicitly treated and the calculation is more realistic than the use of an effective mass model.

There are three types of atoms in the inorganic layer: Pb, horizontal I ( $I_x$  and  $I_y$ ), and vertical I ( $I_z$ ). Figure 3 shows the contribution of each atom type's orbitals to the band structure of  $n = 1$ . At the M point, the valence band maximum (VBM) has 53%  $I_{xy}$   $p$  orbital character and 32% Pb  $s$  orbital character. The contribution of  $I_z$  shows a clear difference from that of  $I_{xy}$ , which is only 15% at the M point and increases to 86% at  $\Gamma$  point. The conduction bands are dominated by Pb, with the conduction band minimum (CBM) having 95% Pb  $p$  orbital character. For this reason, the spin-orbit splitting at the CBM is almost entirely determined by the Pb  $p$  orbitals. These VB and CB orbital compositions are in agreement with previous DFT studies.<sup>15,21</sup> As we go to larger  $n$ , the bands multiply and split due to the strong coupling between the sublayer. As shown in Fig. 3, each band from  $n = 1$  splits into  $n$  subbands for larger  $n$ , which leads to a reduction in the band gap. For large  $n$ , the band structure of the bulk HOIP is regained, as demonstrated in Fig. 2.

The calculated absorption spectra shown in Fig. 4(a) exhibit a strong 1s peak and weak 2s and 3s peaks; the quasiparticle band gap is indicated with a solid circle. As  $n$  increases, both the absorption energy and intensity decrease, approaching the bulk spectrum. For the out-of-plane polarization, the first term of Eq. 11 is zero, and absorption occurs purely due

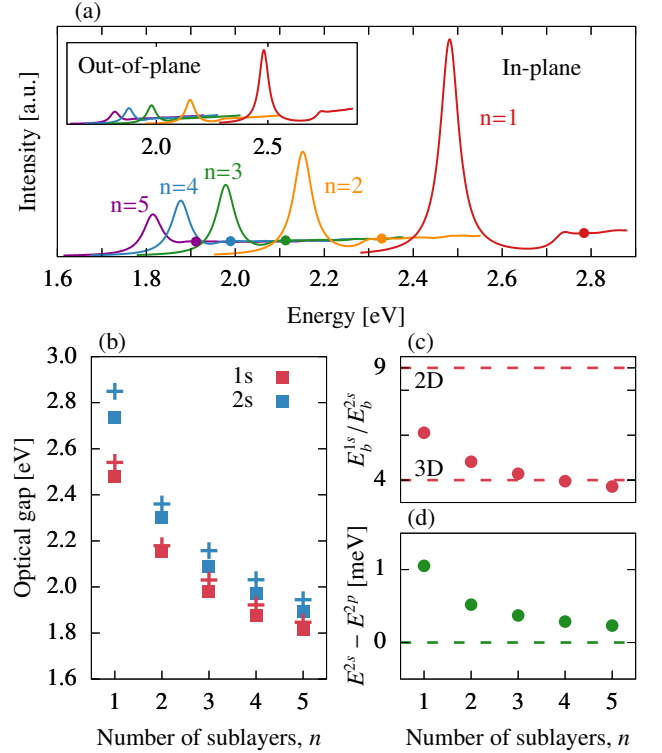


FIG. 4. (a) Excitonic absorption spectra of  $n = 1$  through 5 for in-plane polarized light. Solid dots indicate the band gap of each system. The inset shows the spectra for out-of-plane polarized light, with a magnified scaled compared to the main figure. The spectra are plotted using a Lorentzian line shape with a broadening of 50 meV (full width at half maximum). (b) 1s and 2s peak position as a function of  $n$ . Plus symbols (+) are the experimentally measured values from Ref. 9. (c) Ratio of the 1s and 2s exciton binding energies, where a ratio of 9 or 4 is the prediction of an ideal 2D or 3D hydrogenic model of excitons. (d) Energy difference between the 2s and 2p excitons, showing the degeneracy breaking at small  $n$ .

to the intra-atomic dipole moment. Both polarizations gives a spectrum of similar shape, but the out-of-plane polarization has a much smaller absorption intensity, about 5% that of the in-plane polarization. The energies of the 1s and 2s states are in good agreement with recent experimental measurements,<sup>9</sup> as shown in Fig. 4(b); the discrepancy is less than 0.1 eV for both states and for all values of  $n$ . In our calculations, the 1s exciton binding energies for  $n = 1-5$  are found to be 302 meV, 177 meV, 135 meV, 112 meV, and 97 meV.

Excitons in semiconductors are commonly analyzed with a hydrogenic model of the interacting electron and hole. In three dimensions, this model leads to s-type exciton energy levels with binding energies  $E_b(ms) = \text{Ry}/m^2$ , where the Rydberg constant is  $\text{Ry} = \mu/(2\epsilon^2)$ ,  $\mu$  is the exciton reduced mass, and  $\epsilon$  is a uniform dielectric constant. We can use this model to estimate the prediction of our model for  $n = \infty$ , corresponding to the bulk HOIP. Using  $\mu = 0.10m_0$  (consistent with the band masses reported above) and  $\epsilon = 6.1$ , we find  $E_b^{1s} = 37$  meV. This is in reasonable agreement with experimental values, which range from 7.4 to 50 meV.<sup>29,41,53-57</sup>



Nonhydrogenic behavior in the exciton series<sup>58</sup> can be caused by the combination of nonparabolicity in the band structure, finite-thickness effects, and inhomogeneous dielectric screening. Because the layered HOIPs have some two-dimensional character, we will also compare to the prediction of the 2D hydrogen model of excitons,  $E_b^{ms} = Ry/(m - 1/2)^2$ . The difference between the 2D exciton series and the 3D exciton series can be seen in the ratio of the binding energies of the 1s and 2s states: in 2D  $E_b^{1s}/E_b^{2s} = 4$  and in 3D  $E_b^{1s}/E_b^{2s} = 9$ . In Fig. 4(c), we show this ratio as a function of  $n$ . At  $n = 5$ , the ratio is approximately 4, indicating a conventional 3D exciton within the hydrogenic model. At  $n = 1$ , the ratio is about 6, i.e. larger than 4 but smaller than 9. Therefore, the  $n = 1$  excitons are intermediate between 2D and 3D, displaying a nonhydrogenic Rydberg series. This deviation from the ideal 2D limit of 9 is due to the form of the screened Coulomb potential: the heterogeneous dielectric yields an interaction that is not simply of the form  $1/\epsilon r$ .

Another manifestation of the nonuniform dielectric screening is the breaking of accidental degeneracies in the exciton spectrum. In particular, the angular momentum degeneracy is broken for alternative interactions. In Fig. 4(d), we plot the energy difference  $E^{2s} - E^{2p}$  as a function of  $n$ . At large  $n$ , the 2s and 2p states are nearly degenerate, again indicating conventional 3D hydrogenic exciton behavior. However, the degeneracy is broken at small  $n$ ; in particular, at  $n = 1$  the 2p state is lower in energy by about 1 meV.

Our calculation allows us to quantify the physical mechanisms responsible for the thickness-dependent excitation energies, shown in Fig. 5(a). The  $n$ -dependent band gap, shown with black symbols, can be decomposed into a bulk band gap of 1.67 eV, a carrier confinement energy, and a self-interaction energy due to dielectric contrast.<sup>22</sup> The latter two effects make a significant contribution to the band gap for  $n = 1 - 5$ . At  $n = 1$ , the carrier confinement and dielectric contrast increase the band gap by about 0.7 eV and 0.4 eV, respectively. By  $n = 5$ , the contributions are more modest and amount to about 0.1 eV each. A similar analysis can be done for the 1s excitation energy, which has an additional negative contribution arising from the exciton binding energy. The exciton binding energy almost exactly cancels the band gap increase due to dielectric contrast, which is analogous to the insensitivity of the first excitation energy of transition-metal dichalcogenides to the dielectric of the environment.<sup>59</sup> Therefore, the thickness-dependence of the first excitation energy is largely determined by the confinement energy. However, the wavefunction character of the excited state is excitonic and distinct from that of a confined but noninteracting electron-hole pair. This wavefunction difference will impact various properties and is responsible for the strong, narrow peak observed in the absorption spectrum.

The above result suggests that the band gap can be tuned by the organic spacer but that the 1s excitation energy will be relatively insensitive, assuming that the structure of the inorganic layer is preserved. In Fig. 5(b), we show the band gap and 1s peak energy as a function of the length of the organic molecules used as spacers, ranging from butylammonium (C4) to dodecylammonium (C12). Indeed, for  $n = 1$ , the

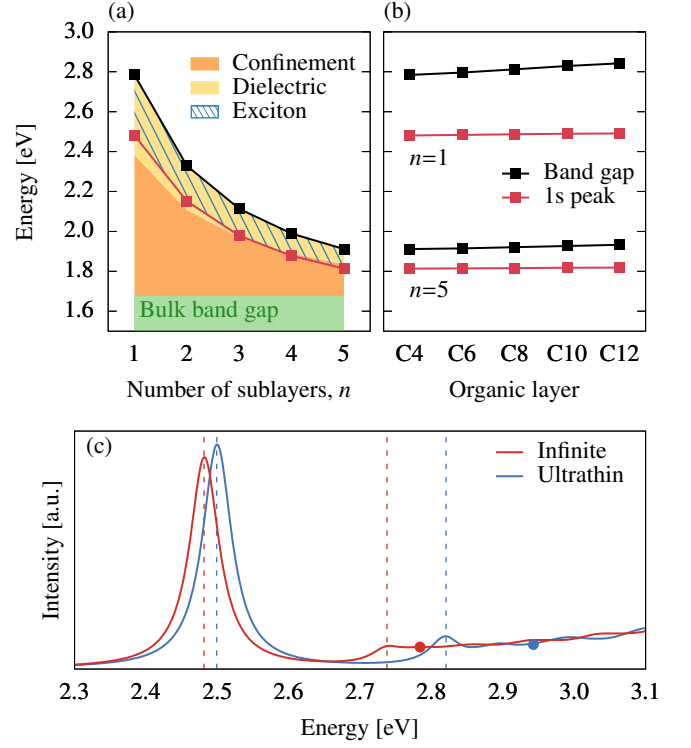


FIG. 5. (a) Band gap (black) and optical gap (red) of the layered HOIP as a function of  $n$ . Orange and yellow shaded area indicate the contribution of the carrier confinement and dielectric contrast self-energy effects to the band gap. Blue striped pattern shows the reduction of the optical gap due to the exciton binding energy. The bulk band gap from Figure 2 is shown as a green shaded area. (b) Band gap and optical gap of the HOIP with  $n = 1$  and 5 as a function of the thickness of the organic layer.  $C_m$  on the x axis indicates the organic cation  $A'^+ = C_m H_{2m+1} NH_3^+$ . (c) Absorption spectra of an infinitely thick  $n = 1$  sample (red line) and an ultrathin exfoliated  $n = 1$  bilayer (blue line). Solid dots are the position of the band gap. Dashed vertical lines indicate the position of the 1s and 2s excitons.

band gap increases by about 0.1 eV by increasing the length of the organic cation, but the 1s energy is essentially unchanged, consistent with early experimental observations.<sup>29</sup> The effect is less dramatic for  $n = 5$ , due to the decreased relevance of the environment surrounding a thick inorganic layer.

An alternative approach to tune the environment of the inorganic layer is through mechanical exfoliation, like can be achieved in layered van der Waals materials and was pursued for HOIPs in Ref. 10. In Fig. 5(c), we compare the spectrum of the  $n = 1$  bulk crystal and an exfoliated  $n = 1$  bilayer on a  $SiO_2/Si$  substrate (modeled with a dielectric constant  $\epsilon = 2.13$ ). This latter ultrathin sample was the one isolated and studied in Ref. 10. The 1s peak of the ultrathin bilayer is located at 2.50 eV, only 20 meV higher than the case of the infinite number of alternating layers and in good agreement with the experimental value of 2.53 eV. The 2s exciton state, having a smaller binding energy, exhibits a larger increase by 90 meV. The band gap increase of 160 meV shows the major consequence of the change in the degree of dielectric con-

trast with a concomitant increase in the exciton binding energy from 302 meV (bulk) to 444 meV (ultrathin). This latter value is in good agreement with the experimentally inferred value of 490 meV.

In conclusion, a semiempirical tight-binding model of the layered HOIPs has been developed and parameterized by ab initio DFT and GW calculations of the 3D HOIP. Our model, together with an approximate solution of the Bethe-Salpeter equation for neutral excitons, provides a tool to analyze the electronic band structure, absorption spectrum, and exciton properties at a low computational cost compared to fully ab initio calculations, which are daunting due to the large unit cell size of the layered HOIPs.

Our results are in good agreement with recently reported experimental measurements. Most importantly, the level of theory enables direct access to the physical properties underlying the observed behaviors. In particular, the carrier confinement, dielectric self-energy, and exciton binding energies have been systematically studied and quantified as a function of  $n$ . We have demonstrated that the 1s and 2s excitons exhibit a nonhydrogenic behavior – with respect to level dispositions and angular momentum degeneracy – that can be controlled by  $n$  and that conventional hydrogenic behavior is recovered at large  $n$ .

This general approach is promising for the investigation of other layered compounds with complex unit cells. Furthermore, the microscopic but affordable tight-binding description will enable the treatment of additional phenomena in the layered HOIPs, which are challenging at the ab initio level. Specifically, we anticipate the study of noncubic phases<sup>7,60</sup> and the Rashba effect,<sup>25,26</sup> lead ion displacements and other sources of disorder,<sup>61–63</sup> and electron-phonon coupling,<sup>64,65</sup> which can impact screening and renormalize the exciton binding energy. Finally, the large exciton binding energies found here suggest the presence of more exotic multi-carrier complexes such as trions<sup>66</sup> and biexcitons,<sup>67–69</sup> work along these lines is currently in progress.

## ACKNOWLEDGMENTS

We thank Shi-Ning Sun for early work on this project. Calculations were performed using resources provided by the University of Chicago Research Computing Center and the Flatiron Institute. This work was supported by the US-Israel Binational Science Foundation Grant BSF-2016362 and by the Air Force Office of Scientific Research under award number FA9550-18-1-0058. The Flatiron Institute is a division of the Simons Foundation.

\* [tim.berkelbach@gmail.com](mailto:tim.berkelbach@gmail.com)

- <sup>1</sup> National Renewable Energy Laboratory. Best Research-Cell Efficiencies. <https://www.nrel.gov/pv/cell-efficiency.html>. Accessed: 2019-08-19.
- <sup>2</sup> Cao, D. H.; Stoumpos, C. C.; Farha, O. K.; Hupp, J. T.; Kanatzidis, M. G. 2D homologous perovskites as light-absorbing materials for solar cell applications. *Journal of the American Chemical Society* **2015**, *137*, 7843–7850.
- <sup>3</sup> Tsai, H. et al. High-efficiency two-dimensional Ruddlesden-Popper perovskite solar cells. *Nature* **2016**, *536*, 312.
- <sup>4</sup> McMeekin, D. P.; Sadoughi, G.; Rehman, W.; Eperon, G. E.; Saliba, M.; Hörlantner, M. T.; Haghighirad, A.; Sakai, N.; Korte, L.; Rech, B.; Johnston, M. B.; Herz, L. M.; Snaith, H. J. A mixed-cation lead mixed-halide perovskite absorber for tandem solar cells. *Science* **2016**, *351*, 151–155.
- <sup>5</sup> Tanaka, K.; Kondo, T. Bandgap and exciton binding energies in lead-iodide-based natural quantum-well crystals. *Science and Technology of Advanced Materials* **2003**, *4*, 599–604.
- <sup>6</sup> Wu, X.; Trinh, M. T.; Zhu, X.-Y. Excitonic many-body interactions in two-dimensional lead iodide perovskite quantum wells. *The Journal of Physical Chemistry C* **2015**, *119*, 14714–14721.
- <sup>7</sup> Stoumpos, C. C.; Cao, D. H.; Clark, D. J.; Young, J.; Rondinelli, J. M.; Jang, J. I.; Hupp, J. T.; Kanatzidis, M. G. Ruddlesden-Popper hybrid lead iodide perovskite 2D homologous semiconductors. *Chemistry of Materials* **2016**, *28*, 2852–2867.
- <sup>8</sup> Stoumpos, C. C.; Soe, C. M. M.; Tsai, H.; Nie, W.; Blancon, J.-C.; Cao, D. H.; Liu, F.; Traoré, B.; Katan, C.; Even, J.; Mohite, A. D.; Kanatzidis, M. G. High members of the 2D Ruddlesden-Popper halide perovskites: synthesis, optical properties, and solar cells of (CH<sub>3</sub> (CH<sub>2</sub>) 3NH<sub>3</sub>) 2 (CH<sub>3</sub>NH<sub>3</sub>) 4Pb<sub>5</sub>I<sub>16</sub>. *Chem* **2017**, *2*, 427–440.
- <sup>9</sup> Blancon, J.-C. et al. Scaling law for excitons in 2D perovskite quantum wells. *Nature communications* **2018**, *9*, 2254.
- <sup>10</sup> Yaffe, O.; Chernikov, A.; Norman, Z. M.; Zhong, Y.; Velauthapillai, A.; van der Zande, A.; Owen, J. S.; Heinz, T. F. Excitons in ultrathin organic-inorganic perovskite crystals. *Physical Review B* **2015**, *92*, 045414.
- <sup>11</sup> Blancon, J.-C. et al. Extremely efficient internal exciton dissociation through edge states in layered 2D perovskites. *Science* **2017**, *355*, 1288–1292.
- <sup>12</sup> Hong, X.; Ishihara, T.; Nurmikko, A. Dielectric confinement effect on excitons in PbI<sub>4</sub>-based layered semiconductors. *Physical Review B* **1992**, *45*, 6961.
- <sup>13</sup> Muljarov, E.; Tikhodeev, S.; Gippius, N.; Ishihara, T. Excitons in self-organized semiconductor/insulator superlattices: PbI<sub>4</sub>-based perovskite compounds. *Physical Review B* **1995**, *51*, 14370.
- <sup>14</sup> Tanaka, K.; Takahashi, T.; Kondo, T.; Umebayashi, T.; Asai, K.; Ema, K. Image charge effect on two-dimensional excitons in an inorganic-organic quantum-well crystal. *Physical Review B* **2005**, *71*, 045312.
- <sup>15</sup> Bala, A.; Deb, A. K.; Kumar, V. Atomic and Electronic Structure of Two-Dimensional Inorganic Halide Perovskites A<sub>n+1</sub>M<sub>n</sub>X<sub>3n+1</sub> (n = 1–6, A = Cs, M = Pb and Sn, and X = Cl, Br, and I) from ab Initio Calculations. *The Journal of Physical Chemistry C* **2018**, *122*, 7464–7473.
- <sup>16</sup> Brivio, F.; Butler, K. T.; Walsh, A.; Van Schilfgaarde, M. Relativistic quasiparticle self-consistent electronic structure of hybrid halide perovskite photovoltaic absorbers. *Physical Review B* **2014**, *89*, 155204.
- <sup>17</sup> Filip, M. R.; Giustino, F. G W quasiparticle band gap of the hybrid organic-inorganic perovskite CH<sub>3</sub>NH<sub>3</sub>PbI<sub>3</sub>: Effect of spin-orbit interaction, semicore electrons, and self-consistency. *Physical Review B* **2014**, *90*, 245145.

- <sup>18</sup> Umari, P.; Mosconi, E.; De Angelis, F. Relativistic GW calculations on CH<sub>3</sub>NH<sub>3</sub>PbI<sub>3</sub> and CH<sub>3</sub>NH<sub>3</sub>SnI<sub>3</sub> perovskites for solar cell applications. *Scientific reports* **2014**, *4*, 4467.
- <sup>19</sup> Filip, M. R.; Verdi, C.; Giustino, F. GW band structures and carrier effective masses of CH<sub>3</sub>NH<sub>3</sub>PbI<sub>3</sub> and hypothetical perovskites of the type APbI<sub>3</sub>: A= NH<sub>4</sub>, PH<sub>4</sub>, AsH<sub>4</sub>, and SbH<sub>4</sub>. *The Journal of Physical Chemistry C* **2015**, *119*, 25209–25219.
- <sup>20</sup> Mosconi, E.; Umari, P.; De Angelis, F. Electronic and optical properties of MAPbX<sub>3</sub> perovskites (X= I, Br, Cl): a unified DFT and GW theoretical analysis. *Physical Chemistry Chemical Physics* **2016**, *18*, 27158–27164.
- <sup>21</sup> Molina-Sánchez, A. Excitonic States in Semiconducting Two-dimensional Perovskites. *ACS Applied Energy Materials* **2018**, *1*, 6361–6367.
- <sup>22</sup> Katan, C.; Mercier, N.; Even, J. Quantum and Dielectric Confinement Effects in Lower-Dimensional Hybrid Perovskite Semiconductors. *Chemical Reviews* **2019**.
- <sup>23</sup> Gao, W.; Gao, X.; Abtew, T. A.; Sun, Y.-Y.; Zhang, S.; Zhang, P. Quasiparticle band gap of organic-inorganic hybrid perovskites: Crystal structure, spin-orbit coupling, and self-energy effects. *Physical Review B* **2016**, *93*, 085202.
- <sup>24</sup> Even, J.; Pedesseau, L.; Katan, C. Understanding quantum confinement of charge carriers in layered 2D hybrid perovskites. *ChemPhysChem* **2014**, *15*, 3733–3741.
- <sup>25</sup> Kim, M.; Im, J.; Freeman, A. J.; Ihm, J.; Jin, H. Switchable S= 1/2 and J= 1/2 Rashba bands in ferroelectric halide perovskites. *Proceedings of the National Academy of Sciences* **2014**, *111*, 6900–6904.
- <sup>26</sup> Zheng, F.; Tan, L. Z.; Liu, S.; Rappe, A. M. Rashba spin-orbit coupling enhanced carrier lifetime in CH<sub>3</sub>NH<sub>3</sub>PbI<sub>3</sub>. *Nano letters* **2015**, *15*, 7794–7800.
- <sup>27</sup> Boyer-Richard, S.; Katan, C.; Traore, B.; Scholz, R.; Jancu, J.-M.; Even, J. Symmetry-based tight binding modeling of halide perovskite semiconductors. *The Journal of Physical Chemistry Letters* **2016**, *7*, 3833–3840.
- <sup>28</sup> Oku, T. *Solar Cells-New Approaches and Reviews*; IntechOpen, 2015.
- <sup>29</sup> Ishihara, T.; Takahashi, J.; Goto, T. Optical properties due to electronic transitions in two-dimensional semiconductors (C<sub>n</sub>H<sub>2</sub>n+1NH<sub>3</sub>)<sub>2</sub>PbI<sub>4</sub>. *Physical Review B* **1990**, *42*, 11099.
- <sup>30</sup> Knutson, J. L.; Martin, J. D.; Mitzi, D. B. Tuning the band gap in hybrid tin iodide perovskite semiconductors using structural templating. *Inorganic chemistry* **2005**, *44*, 4699–4705.
- <sup>31</sup> Mayers, M. Z.; Tan, L. Z.; Egger, D. A.; Rappe, A. M.; Reichman, D. R. How lattice and charge fluctuations control carrier dynamics in halide perovskites. *Nano letters* **2018**, *18*, 8041–8046.
- <sup>32</sup> Giannozzi, P. et al. Advanced capabilities for materials modelling with QUANTUM ESPRESSO. *Journal of Physics: Condensed Matter* **2017**, *29*, 465901.
- <sup>33</sup> Perdew, J. P.; Burke, K.; Ernzerhof, M. Generalized gradient approximation made simple. *Physical Review Letters* **1996**, *77*, 3865.
- <sup>34</sup> Mostofi, A. A.; Yates, J. R.; Pizzi, G.; Lee, Y.-S.; Souza, I.; Vanderbilt, D.; Marzari, N. An updated version of wannier90: A tool for obtaining maximally-localised Wannier functions. *Computer Physics Communications* **2014**, *185*, 2309–2310.
- <sup>35</sup> Even, J.; Pedesseau, L.; Jancu, J.-M.; Katan, C. Importance of spin-orbit coupling in hybrid organic/inorganic perovskites for photovoltaic applications. *The Journal of Physical Chemistry Letters* **2013**, *4*, 2999–3005.
- <sup>36</sup> Hedin, L. New method for calculating the one-particle Green's function with application to the electron-gas problem. *Physical Review* **1965**, *139*, A796.
- <sup>37</sup> Strinati, G.; Mattausch, H. J.; Hanke, W. Dynamical Correlation Effects on the Quasiparticle Bloch States of a Covalent Crystal. *Physical Review Letters* **1980**, *45*, 290–294.
- <sup>38</sup> Strinati, G.; Mattausch, H. J.; Hanke, W. Dynamical aspects of correlation corrections in a covalent crystal. *Physical Review B* **1982**, *25*, 2867–2888.
- <sup>39</sup> Hybertsen, M. S.; Louie, S. G. First-principles theory of quasiparticles: calculation of band gaps in semiconductors and insulators. *Physical Review Letters* **1985**, *55*, 1418.
- <sup>40</sup> Hybertsen, M. S.; Louie, S. G. Electron correlation in semiconductors and insulators: Band gaps and quasiparticle energies. *Physical Review B* **1986**, *34*, 5390.
- <sup>41</sup> Miyata, A.; Mitioglu, A.; Plochocka, P.; Portugall, O.; Wang, J. T.-W.; Stranks, S. D.; Snaith, H. J.; Nicholas, R. J. Direct measurement of the exciton binding energy and effective masses for charge carriers in organic-inorganic tri-halide perovskites. *Nature Physics* **2015**, *11*, 582.
- <sup>42</sup> Guseinov, R. Coulomb interaction and excitons in a superlattice. *physica status solidi (b)* **1984**, *125*, 237–243.
- <sup>43</sup> Cavalcante, L.; Chaves, A.; Van Duppen, B.; Peeters, F.; Reichman, D. Electrostatics of electron-hole interactions in van der Waals heterostructures. *Physical Review B* **2018**, *97*, 125427.
- <sup>44</sup> Brus, L. A simple model for the ionization potential, electron affinity, and aqueous redox potentials of small semiconductor crystallites. *The Journal of chemical physics* **1983**, *79*, 5566–5571.
- <sup>45</sup> Kumagai, M.; Takagahara, T. Excitonic and nonlinear-optical properties of dielectric quantum-well structures. *Physical Review B* **1989**, *40*, 12359.
- <sup>46</sup> Sham, L. J.; Rice, T. M. Many-Particle Derivation of the Effective-Mass Equation for the Wannier Exciton. *Physical Review* **1966**, *144*, 708–714.
- <sup>47</sup> Hanke, W.; Sham, L. J. Many-particle effects in the optical spectrum of a semiconductor. *Physical Review B* **1980**, *21*, 4656–4673.
- <sup>48</sup> Strinati, G. Effects of dynamical screening on resonances at inner-shell thresholds in semiconductors. *Physical Review B* **1984**, *29*, 5718–5726.
- <sup>49</sup> Albrecht, S. Excitonic Effects in the Optical Properties. *phys. stat. sol. (a)* **1998**, *170*, 189.
- <sup>50</sup> Rohlfing, M.; Louie, S. G. Electron-hole excitations and optical spectra from first principles. *Physical Review B* **2000**, *62*, 4927.
- <sup>51</sup> Ridolfi, E.; Lewenkopf, C. H.; Pereira, V. M. Excitonic structure of the optical conductivity in MoS<sub>2</sub> monolayers. *Physical Review B* **2018**, *97*, 205409.
- <sup>52</sup> Pedersen, T. G.; Pedersen, K.; Kristensen, T. B. Optical matrix elements in tight-binding calculations. *Physical Review B* **2001**, *63*, 201101.
- <sup>53</sup> Ziffer, M. E.; Mohammed, J. C.; Ginger, D. S. Electroabsorption spectroscopy measurements of the exciton binding energy, electron-hole reduced effective mass, and band gap in the perovskite CH<sub>3</sub>NH<sub>3</sub>PbI<sub>3</sub>. *ACS Photonics* **2016**, *3*, 1060–1068.
- <sup>54</sup> Phuong, L. Q.; Nakaike, Y.; Wakamiya, A.; Kanemitsu, Y. Free excitons and exciton-phonon coupling in CH<sub>3</sub>NH<sub>3</sub>PbI<sub>3</sub> single crystals revealed by photocurrent and photoluminescence measurements at low temperatures. *The Journal of Physical Chemistry Letters* **2016**, *7*, 4905–4910.
- <sup>55</sup> Yang, Y.; Yang, M.; Li, Z.; Crisp, R.; Zhu, K.; Beard, M. C. Comparison of recombination dynamics in CH<sub>3</sub>NH<sub>3</sub>PbBr<sub>3</sub> and CH<sub>3</sub>NH<sub>3</sub>PbI<sub>3</sub> perovskite films: influence of exciton binding energy. *The Journal of Physical Chemistry Letters* **2015**, *6*, 4688–4692.
- <sup>56</sup> Hirasawa, M.; Ishihara, T.; Goto, T.; Uchida, K.; Miura, N. Magnetoabsorption of the lowest exciton in perovskite-type compound (CH<sub>3</sub>NH<sub>3</sub>)PbI<sub>3</sub>. *Physica B: Condensed Matter* **1994**, *201*, 427–430.

- <sup>57</sup> Tanaka, K.; Takahashi, T.; Ban, T.; Kondo, T.; Uchida, K.; Miura, N. Comparative study on the excitons in lead-halide-based perovskite-type crystals  $\text{CH}_3\text{NH}_3\text{PbBr}_3$   $\text{CH}_3\text{NH}_3\text{PbI}_3$ . *Solid state communications* **2003**, *127*, 619–623.
- <sup>58</sup> Chernikov, A.; Berkelbach, T. C.; Hill, H. M.; Rigosi, A.; Li, Y.; Aslan, O. B.; Reichman, D. R.; Hybertsen, M. S.; Heinz, T. F. Exciton binding energy and nonhydrogenic Rydberg series in monolayer WS<sub>2</sub>. *Physical Review Letters* **2014**, *113*, 076802.
- <sup>59</sup> Cho, Y.; Berkelbach, T. C. Environmentally sensitive theory of electronic and optical transitions in atomically thin semiconductors. *Physical Review B* **2018**, *97*, 041409.
- <sup>60</sup> Menéndez-Proupin, E.; Palacios, P.; Wahnón, P.; Conesa, J. Self-consistent relativistic band structure of the  $\text{CH}_3\text{NH}_3\text{PbI}_3$  perovskite. *Physical Review B* **2014**, *90*, 045207.
- <sup>61</sup> Even, J.; Pedesseau, L.; Katan, C. Analysis of multivalley and multibandgap absorption and enhancement of free carriers related to exciton screening in hybrid perovskites. *The Journal of Physical Chemistry C* **2014**, *118*, 11566–11572.
- <sup>62</sup> Motta, C.; Mandal, P.; Sanvito, S. Effects of molecular dipole orientation on the exciton binding energy of  $\text{CH}_3\text{NH}_3\text{PbI}_3$ . *Physical Review B* **2016**, *94*, 045202.
- <sup>63</sup> Smith, M. D.; Pedesseau, L.; Kepenekian, M.; Smith, I. C.; Katan, C.; Even, J.; Karunadasa, H. I. Decreasing the electronic confinement in layered perovskites through intercalation. *Chemical science* **2017**, *8*, 1960–1968.
- <sup>64</sup> Wu, X.; Trinh, M. T.; Niesner, D.; Zhu, H.; Norman, Z.; Owen, J. S.; Yaffe, O.; Kudisch, B. J.; Zhu, X.-Y. Trap states in lead iodide perovskites. *Journal of the American Chemical Society* **2015**, *137*, 2089–2096.
- <sup>65</sup> Guo, Z.; Wu, X.; Zhu, T.; Zhu, X.; Huang, L. Electron–phonon scattering in atomically thin 2D perovskites. *ACS nano* **2016**, *10*, 9992–9998.
- <sup>66</sup> Zahra, H.; Jaziri, S. Screened excitons and trions by free carriers in the two-dimensional perovskite structure. *Physica E: Low-dimensional Systems and Nanostructures* **2019**, *113*, 181–187.
- <sup>67</sup> Kato, Y.; Ichii, D.; Ohashi, K.; Kunugita, H.; Ema, K.; Tanaka, K.; Takahashi, T.; Kondo, T. Extremely large binding energy of biexcitons in an organic–inorganic quantum-well material ( $\text{C}_4\text{H}_9\text{NH}_3$ )<sub>2</sub>PbBr<sub>4</sub>. *Solid state communications* **2003**, *128*, 15–18.
- <sup>68</sup> Elkins, M. H.; Pensack, R.; Proppe, A. H.; Voznyy, O.; Quan, L. N.; Kelley, S. O.; Sargent, E. H.; Scholes, G. D. Biexciton Resonances Reveal Exciton Localization in Stacked Perovskite Quantum Wells. *The Journal of Physical Chemistry Letters* **2017**, *8*, 3895–3901.
- <sup>69</sup> Thouin, F.; Neutzner, S.; Cortecchia, D.; Dragomir, V. A.; Soci, C.; Salim, T.; Lam, Y. M.; Leonelli, R.; Petrozza, A.; Kandada, A. R. S.; Silva, C. Stable biexcitons in two-dimensional metal-halide perovskites with strong dynamic lattice disorder. *Physical Review Materials* **2018**, *2*, 034001.